DREMnet: An Interpretable Denoising Framework for Semi-Airborne Transient Electromagnetic Signal

Shuang Wang, Ming Guo, Xuben Wang, Fei Deng, Lifeng Mao, Bin Wang and Wenlong Gao

Abstract—The semi-airborne transient electromagnetic method (SATEM) is capable of conducting rapid surveys over large-scale and hard-to-reach areas. However, the acquired signals are often contaminated by complex noise, which can compromise the accuracy of subsequent inversion interpretations. Traditional denoising techniques primarily rely on parameter selection strategies, which are insufficient for processing field data in noisy environments. With the advent of deep learning, various neural networks have been employed for SATEM signal denoising. However, existing deep learning methods typically use single-mapping learning approaches that struggle to effectively separate signal from noise. These methods capture only partial information and lack interpretability. To overcome these limitations, we propose an interpretable decoupled representation learning framework, termed DREMnet, that disentangles data into content and context factors, enabling robust and interpretable denoising in complex conditions. To address the limitations of CNN and Transformer architectures, we utilize the RWKV architecture for data processing and introduce the Contextual-WKV mechanism, which allows unidirectional WKV to perform bidirectional signal modeling. Our proposed Covering Embedding technique retains the strong local perception of convolutional networks through stacked embedding. Experimental results on test datasets demonstrate that the DREMnet method outperforms existing techniques, with processed field data that more accurately reflects the theoretical signal, offering improved identification of subsurface electrical structures.

Index Terms—Transient Electromagnetic Signal Denoising, Disentangled Representation Learning, RWKV, Neural network.

I. INTRODUCTION

THE semi-airborne transient electromagnetic method (SATEM) is an emerging electromagnetic exploration technique in which the transmitter is deployed on the ground, while the receiver is mounted on an airborne platform [1]. By performing inversion on the received secondary field signals, it enables accurate extraction of subsurface electrical structures [2]. SATEM is highly effective for surveying large and inaccessible areas and has been widely applied in mineral resource exploration, groundwater investigation, as well as environmental protection and geological hazard assessment [3]–[6].

Since the system conducts observations while in motion, significant noise is inevitably introduced. In SATEM data, typical noise can be divided into natural electromagnetic noise, cultural electromagnetic noise, motion-induced noise [7], [8], and platform noise [9]. Natural noise typically manifests as short-term pulses, primarily caused by thunder and lightning [10]. Cultural electromagnetic noise refers to stable power line noise and very low-frequency (VLF) radio interference encountered during observations [11]. In some application scenarios, intense pulse interference may occur, such as ore concentration areas [12]. Motion-induced noise is a non-stationary noise generated as the sensor moves with the airborne platform, caused by irregularities in the geomagnetic field. Compared to other noise sources, motion-induced noise is characterized by large amplitude, wide distribution, and low frequency [13], [14]. Additionally, due to the long observation distance, the received signal strength is relatively weak. The combination of weak signals and complex noise presents substantial challenges in SATEM data processing, making noise suppression and removal crucial steps in the process.

Current SATEM data denoising methods can be broadly divided into two categories: traditional filtering techniques and deep learning-based approaches. Traditional filter-based methods primarily rely on empirical parameter settings, which are determined by observing the physical characteristics of the acquired data. For instance, Lv *et al.* [15] proposed a denoising scheme combining wavelet threshold filtering with adaptive singular value decomposition filtering. Sun *et al.* [16] introduced a simple yet effective single-period polynomial fitting method to remove motion noise from secondary field data. Yang *et al.* [17] developed an overdetermined linear system for late-time motion noise in semi-airborne transient electromagnetic data, based on Fourier series, which was then solved using least-squares inversion for denoising. Ma *et al.* [18] derived a calculation formula for mutual inductance coupling between the transmitter and receiver, and subsequently proposed a hybrid correction scheme using a two-stage strategy to correct receiver noise. Most traditional methods rely heavily on the selection of empirical parameters, which requires significant expertise from data processors [19]. Moreover, these methods are generally more suitable for data with low noise levels and often struggle to effectively suppress complex, high-noise field data.

Deep learning-based methods exploit the powerful learning and modeling capabilities of neural networks to perform denoising, offering advantages such as end-to-end processing, high speed, and strong noise reduction performance [20]–[23]. For example, Chen *et al.* [24] innovatively transformed one-dimensional signals into two-dimensional sequences and applied an image denoising network to transient electromagnetic data, achieving promising results. Pan *et al.* [25] designed a one-dimensional denoising network based on the encoder

Shuang Wang, Ming Guo, X. Wang, L. Mao and W. Gao are with the Key Laboratory of Earth Exploration and Information Techniques, Ministry of Education, College of Geophysics, Chengdu University of Technology, Chengdu 610059, China (e-mail: wangs@stu.cdut.edu.cn; mingguo_cdut@163.com; wxb@cdut.edu.cn; maolifeng07@cdut.edu.cn; gaowenlong@stu.cdut.edu.cn).

Fei Deng, and Bin Wang are with the College of Computer Science and Cyber Security, Chengdu University of Technology, Chengdu 610059, China (e-mail: dengfei@cdut.edu.cn; woldier@foxmail.com).
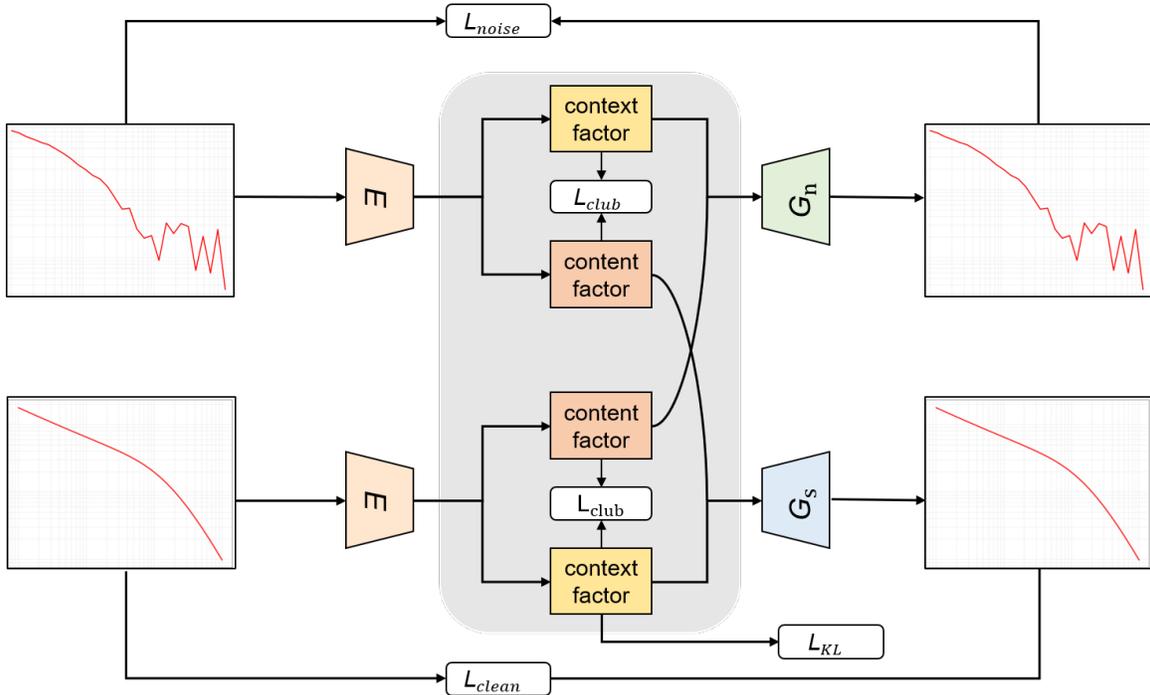
Fig. 1. The overall framework, the data is encoded by the encoder E into content factors and context factors. G_s is used to obtain an accurate clean signal, while G_n ensures the correctness of the disentangled representations.

structure of the Vision Transformer [26], effectively reducing noise in transient electromagnetic data. Deng *et al.* [27] proposed a denoising method using VDM, which introduced constraint conditions to guide the diffusion model [28] and achieve the desired denoising results. Lin *et al.* [29] introduced a recurrent self-coding neural network (RSCN) specifically designed for one-stop noise suppression along an entire survey line.

The aforementioned methods rely on predicting either noise or signal, representing a single-mapping learning approach. This singular representation often struggles to effectively separate signal from noise [30], resulting in representations that contain both components. Consequently, these methods face challenges in isolating noise and signal when processing complex field data and can only capture partial information from the signal. Furthermore, convolutional network structures, due to their inherent limitations [31], are insufficient for global modeling of time-series signals. In contrast, Transformer and VDM methods are computationally intensive, with their memory and computational complexity increasing quadratically with sequence length, rendering standard Transformers impractical and costly for long-sequence signals. Additionally, existing solutions are typically end-to-end mapping approaches, which lack interpretability.

To address the aforementioned issues and enhance interpretability, we propose an interpretable disentangled representation learning framework, termed DREMnet. This framework separates the data into content and context factors, enabling robust denoising of SATEM data under complex conditions while improving interpretability. To overcome the limitations of CNN and Transformer architectures, we adopt the Re-

ceptance Weighted Key Value (RWKV) [32], [33] architecture for data processing. The original RWKV's WKV [34] attention mechanism is unidirectional; however, for SATEM signals, the current signal is correlated with both preceding and succeeding signals. To facilitate bidirectional modeling, we introduce the Contextual-WKV mechanism, which extends the unidirectional WKV to support bidirectional signal modeling. To preserve the strong local perception capability of convolutional networks, we propose the Covering Embedding technique, which incorporates overlapping embeddings to ensure each token retains information directly relevant to it. Experimental results on the test set demonstrate that the DREMnet method achieves superior denoising performance. Furthermore, inversion results from processed field data indicate that the DREMnet-processed data closely align with theoretical signals, providing a more accurate reflection of subsurface features.

The contributions of this paper are as follows:

1. We propose an interpretable disentangled representation learning framework that decomposes data into content and context factors, enabling robust and interpretable denoising of SATEM data under complex conditions.

2. The proposed Contextual-WKV mechanism extends the unidirectional WKV to support bidirectional signal modeling. Additionally, we introduce Covering Embedding, which overlays embeddings to ensure each token retains information directly relevant to it. This approach effectively mitigates the limitations of CNN and Transformer architectures while preserving their advantages.

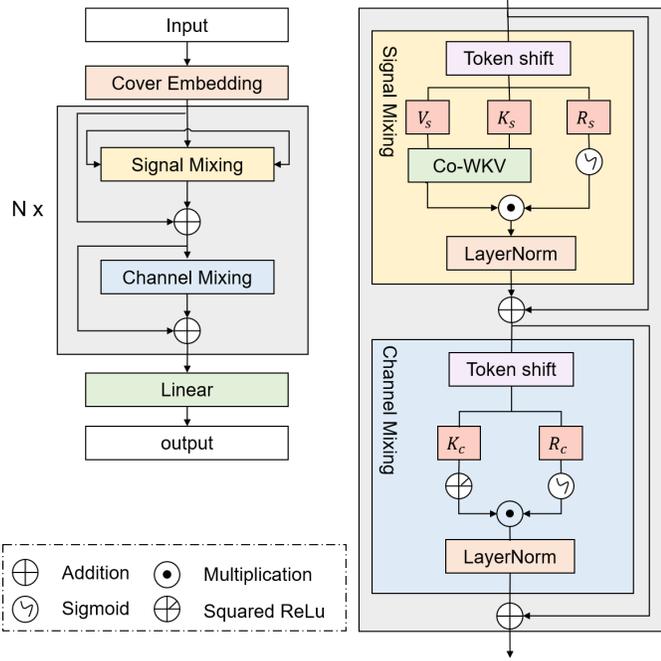3. Comprehensive experiments demonstrate that the DREMnet method achieves superior denoising performance. The

Fig. 2. The Encoder and Decoder architecture (on the left) and the DR block (on the right) consist of the signal mixing module and the channel mixing module.

processed field data more closely aligns with theoretical signals, providing a more accurate representation of subsurface electrical structures.

II. METHOD

A. Framework Overview

The observed SATEM signal is typically represented as the sum of two components: noise and the response signal:

$$y = s + n \tag{1}$$

where y is the observed signal, s is the response signal, and n represents the noise. Most deep learning denoising methods focus on single representation learning, where the neural network predicts either the noise or the signal. However, residual learning has been shown to offer superior performance [35]. As a result, most networks adopt noise prediction to enable denoising, represented as:

$$s' = s + n - \text{net}(s + n) \tag{2}$$

Where, $\text{net}(s + n)$ represents the neural network's prediction of the noise in the observed signal y. The training objective of the network is to minimize $n - \text{net}(s + n)$. This single-representation learning approach exhibits inherent limitations in separating noise from signals. In contrast, decoupled representation learning models critical data representations by disentangling information into task-relevant and task-irrelevant factors [36]. For denoising applications, the informative signal components are considered task-relevant factors, while the noise components are task-irrelevant factors. Therefore, applying decoupled representation learning to separate data into content and context factors enables robust and interpretable
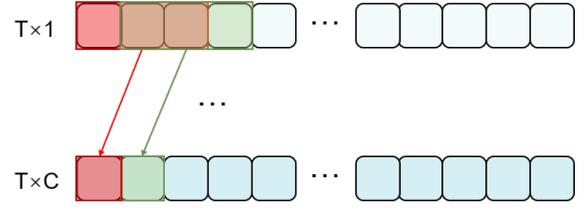

Fig. 3. Cover Embedding, as illustrated in the case where the cover length is 3, combines the current signal data along with the next two signal data into a token with a dimension of C.

denoising under complex conditions. The overall framework is shown in Fig. 1.

The DREMnet framework consists of three core components: an encoder E, a denoising decoder G_s, and a representation decoder G_n. The encoder E encodes input data into content and context factors. The denoising decoder G_s reconstructs clean signals by decoding a combination of content factors extracted from noisy signals and context factors derived from noise-free references. The representation decoder G_n decodes the combination of content and context factors into the corresponding signals, ensuring the correctness of the decoupled representation.

Given the collected data x, the encoder E encodes it into a pair of disentangled representations:

$$Z_s, Z_n = E(x) \tag{3}$$

Here, Z_s represents the content factors, and Z_n represents the context factors. To ensure the distributions of Z_s and Z_n are fully separated, we employ a mutual information upper bound estimator, CLUB [37], since the distributions of the signal and noise are entirely distinct. Intuitively, because the clean signal contains no noise, we treat the distribution of the context factors of the clean signal as a zero vector, $Z_n = 0$, and use KL divergence to constrain its distribution. During training, the encoder E encodes both the noisy signal n and the clean signal s. We aim for the network to correctly learn the disentangled representations: $\{Z_s^1, Z_n^1\} = E(n)$ and $\{Z_s^2, Z_n^2\} = E(s)$. The content factors Z_s^1 and Z_s^2 should follow the same distribution, indicating that the content factor representations are similar, while the context factors should differ, as the clean signal contains no noise. Consequently, we swap the context factors between the two representations and use the representation decoder to decode them. Decoding (Z_s^2, Z_n^1) should yield the noisy signal, confirming that the data has been fully disentangled. Finally, the denoising decoder G_s decodes the combination of content and context factors to produce the denoised signal.

$$s = G_s(Z_s^1, Z_n^2) \tag{4}$$

The overall loss function is:

$$L = L_{clean} + L_{noise} + L_{KL} \tag{5}$$

$$L_{clean} = ||G_s(Z_s^1, Z_n^2) - s||^2 \tag{6}$$

$$L_{noise} = ||G_n(Z_s^2, Z_n^1) - n||^2 \tag{7}$$

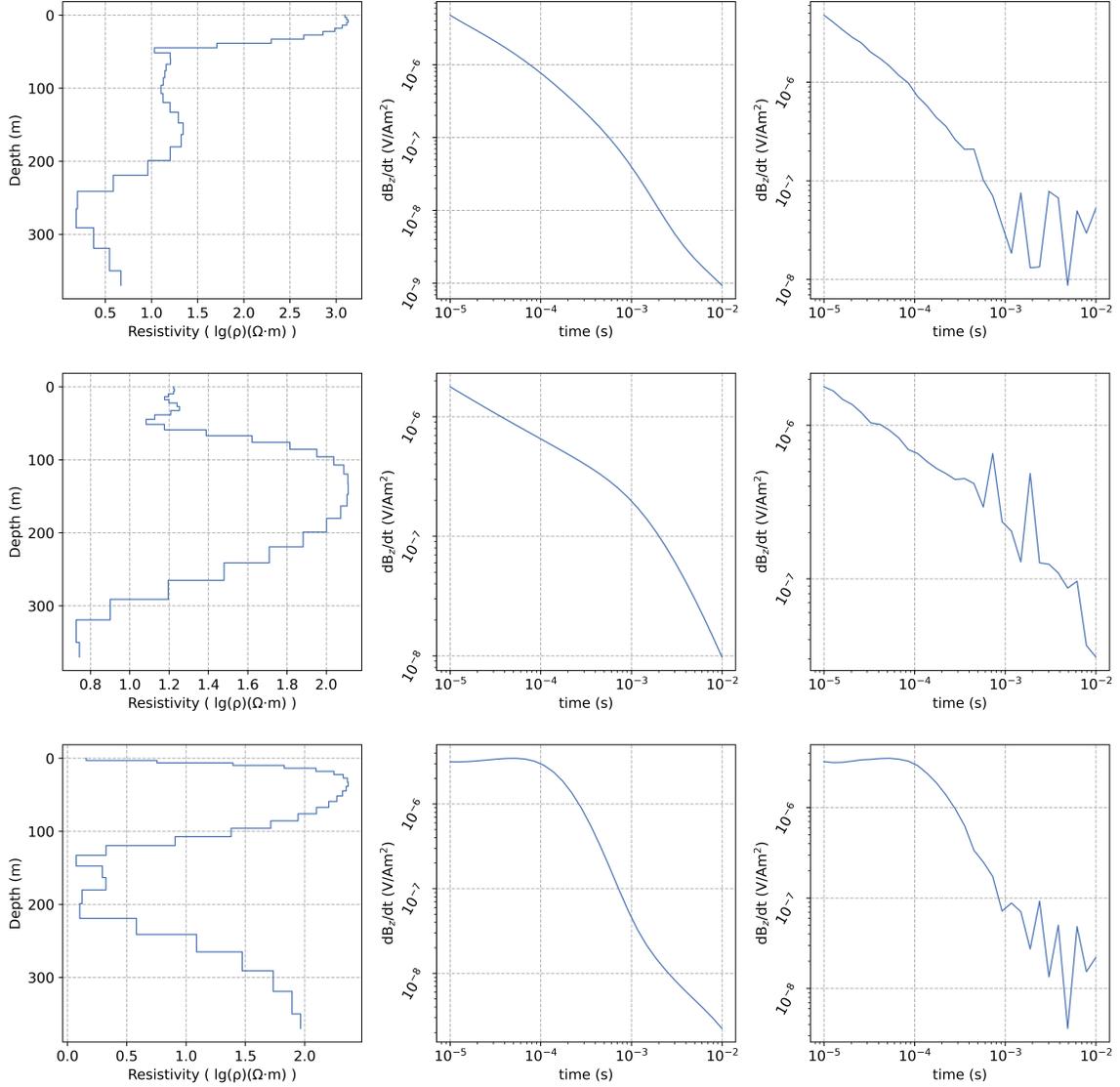$$L_{KL} = (\mu^2 + \sigma^2 - log(\sigma^2) - 1) \tag{8}$$

Fig. 4. Model (left), forward modeling data (center), noise-added data (right).

where μ and σ denote the mean and standard deviation of $\mathbf{Z}\mathbf{s}^2$, respectively.

B. RWKV-Based Encoder and Decoder

To overcome the limitations of CNN and Transformer architectures [38], [39], we employ the RWKV architecture for data processing. Both the encoder and decoder adopt the same architecture, as illustrated in Fig. 2. After the SATEM signal is input, it first passes through a cover embedding module (detailed in the Cover Embedding section) to enhance local signal information. The signal is then processed through N DR blocks before being passed through a linear layer to produce the output. Our design retains the advantages of RWKV with only necessary modifications.

The DR blocks comprises a signal mixing module and a channel mixing module. The signal mixing module functions as the attention mechanism, enabling linear global attention calculations. Meanwhile, the channel mixing module facilitates the fusion of token features across channels.

The signal mixing module can perform linear global attention on the signal processed through Cover Embedding $x \in \mathbb{R}^{T \times C}$. Where, T represents the signal length, and C denotes the embedding dimension. The signal mixing module first performs a token shift, following the original design of RWKV without any modifications. The resulting x_s after the token shift is then processed through three linear layers to obtain R_s, K_s and V_s.

$$R_s = x_s W_r, K_s = x_s W_k, V_s = x_s W_v \qquad (9)$$

Where W_r, W_k and W_v represent the weights of the three linear layers, then use Co-WKV (see the Contextual-WKV subsection) to perform global linear attention calculations.

$$wkv_t = Co - wkv(K_s, V_s) \qquad (10)$$

Finally, the attention results are adjusted using R_s to produce the output.

The channel mixing module performs feature fusion on tokens across channels, processing the token sequence after
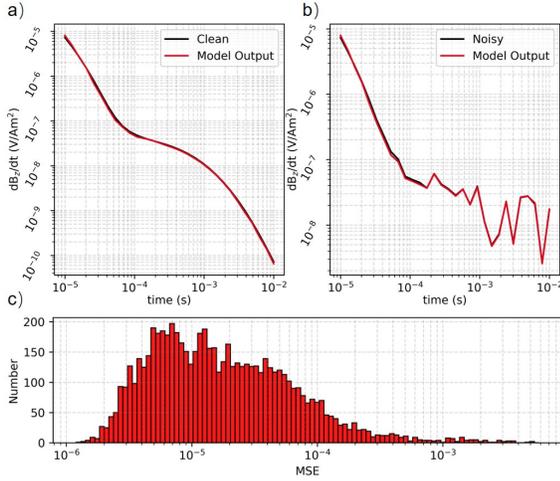
Fig. 5. The clean signal s is disentangled into signal factors Z_s^1 and noise factors Z_n^1, while the noisy signal n is disentangled into signal factors Z_s^2 and noise factors Z_n^2. (a) The clean signal is decoded using (Z_s^2, Z_n^1). (b) The noisy signal is decoded using (Z_s^1, Z_n^2). (c) The MSE statistics of the decoded data from (Z_s^1, Z_n^2) on the test set, compared to the noisy signal.

signal mixing, $x \in \mathbb{R}^{T \times C}$. Channel mixing also applies a token shift, followed by two linear layers to obtain R_c and K_c, ultimately producing the output through feature fusion.

C. Contextual-wkv

The original RWKV's WKV attention mechanism is unidirectional, which limits the attention receptive field and does not provide global attention. Therefore, we utilize Contextual-WKV (Co-WKV), an improved WKV attention mechanism, to enable global attention computation. Given the inputs $K_s \in \mathbb{R}^{T \times C}$ and $V_s \in \mathbb{R}^{T \times C}$, the attention computation result wkv_t for the t-th token can be expressed as:

$$wkv_t = \frac{\sum_{i=0,i\neq t}^{T-1} e^{-(|t-i|-1)w+k_i}v_i + e^{u+k_t}v_t}{\sum_{i=0,i\neq t}^{T-1} e^{-(|t-i|-1)w+k_i} + e^{u+k_t}} \quad (11)$$

Where, T represents the number of tokens, and $k_i \in \mathbb{R}^C$ and $v_i \in \mathbb{R}^C$ denote the i-th token in $K_s \in \mathbb{R}^{T \times C}$ and $V_s \in \mathbb{R}^{T \times C}$, respectively. $w \in \mathbb{R}^C$ and $u \in \mathbb{R}^C$ are two learnable parameters representing the decay weight of the relative position bias $-(|t-i|-1)$ and the reward for the current t-th token. Therefore, wkv_t is essentially the weighted sum of v_1 to v_t, with the weights determined by k_i, the relative position bias, and the parameters w and u.

D. Cover Embedding

To ensure that each token contains information relevant to its directly associated data and to endow DREMnet with the strong local perceptual advantages of convolutional networks, we applied Cover Embedding to the input signal. Cover Embedding is a type of overlapping embedding, as illustrated in Fig. 3. For an input signal of length T and a cover length of n, Cover Embedding combines the current signal data with the subsequent $n-1$ signal data into a token with a dimension of C. Consequently, the final signal of length T is transformed

into a token sequence $T \times C$ after applying Cover Embedding.

III. EXPERIMENTS

A. Evaluation Metrics:

To quantitatively assess the quality of the denoising results, we selected three commonly used metrics: mean squared error (MSE), signal-to-noise ratio (SNR), and structural similarity index measure (SSIM). MSE measures the error between the denoised results and the ground truth, and its calculation formula is as follows:

$$MSE = \frac{1}{n} \sum_{i=1}^{n} (x_i^d - x_i^t)^2 \quad (12)$$

Where x_i^d represents the data denoised by the network, x_i^t represents the ground truth, and the closer the MSE value is to 0, the closer the denoising result is to the ground truth. SNR measures the quality of the denoising result, calculated by the following formula:

$$SNR = 10 log_{10} \frac{||x_d||_F^2}{||x_t - x_d||_F^2} \quad (13)$$

Where x_d represents the data after denoising by the network, x_t denotes the ground truth, and $||\cdot||_F$ represents the Frobenius norm. A larger SNR value indicates a higher quality of denoising. The SSIM measures the structural consistency of the denoised results, and its calculation formula is as follows:

$$SSIM = \frac{(2u_d u_t + c_1)(2\sigma_{dt} + c_2)}{(u_d^2 + u_t^2 + c_1)(\sigma_d^2 + \sigma_t^2 + c_2)} \quad (14)$$

Where u_d is the mean of the denoised result, u_t is the mean of the ground truth, σ_{dt} is the covariance between the denoised result and the ground truth, σ_d is the variance of the denoised result, and σ_t is the variance of the ground truth. The constants c_1 and c_2 are introduced to avoid numerical instability. A SSIM value closer to 1 indicates that the denoised result is closer to the ground truth.

B. Dataset

We utilized the large resistivity model database (RMD) developed by [40], which contains a variety of geologically plausible and geophysically resolvable subsurface structures. The database comprises approximately one million resistivity models, with resistivity values ranging from 1 to 2000 ohm-meters, consisting of 30 layers and a maximum depth of 500 meters. Each model adheres to physical constraints. RMD has been shown to improve performance and generalization while also enhancing the consistency and reliability of deep learning models [41].

We conducted one-dimensional forward modeling on the database to obtain the corresponding forward responses. Then, we introduced noise into the forward response data. Part of the noise was derived from actual field measurements, which includes motion-induced noise, nearby or moderately distant sferics noise, cultural and natural electromagnetic noise. As a type of incidental impulse noise, the amount of extraction of
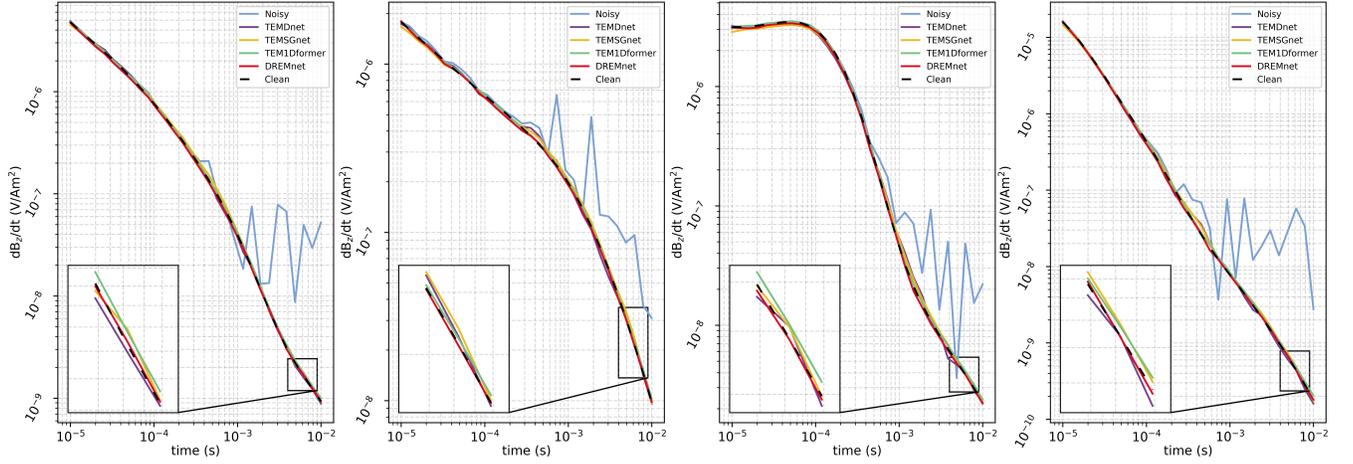
Fig. 6. Four examples of denoising results for the four methods on the test dataset.
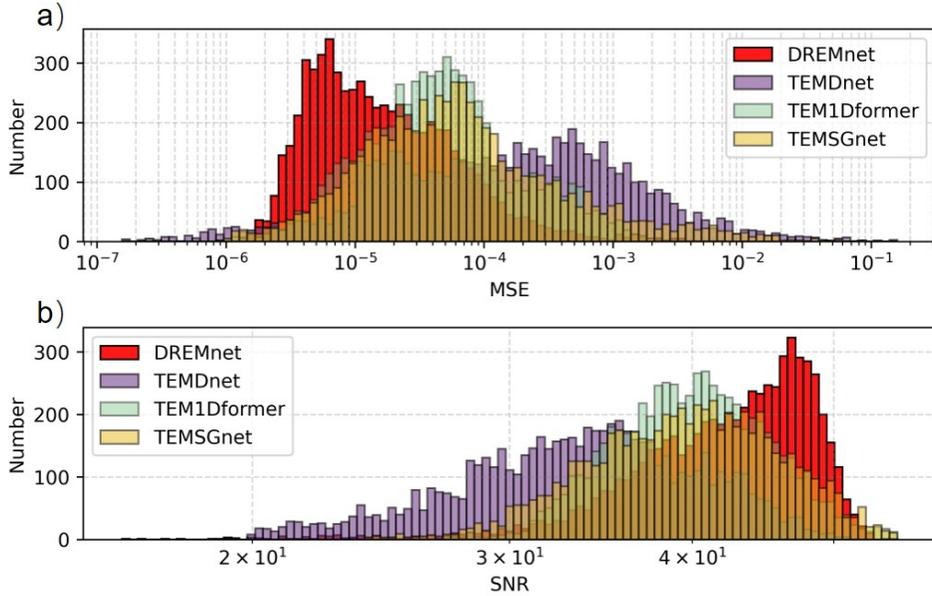

Fig. 7. (a) MSE statistics of the denoising results across the entire test set. (b) SNR statistics of the denoising results across the entire test set.

the nearby or moderately distant sferics noise was relatively small, while another part was Gaussian noise, as complex field noise distributions are often approximated by a Gaussian distribution [24]. For the remaining noise, we selected a simulation method that has been shown to closely replicate actual noise [42], which is defined as:

$$s_n = s + N(0,1)[STD^2 + (\frac{n}{s})^2]^{\frac{1}{2}}s \quad (15)$$

Where, s_n represents the obtained noisy signal, and s is the forward theoretical data. $N(0,1)$ denotes the standard Gaussian distribution. STD is the uniform noise, and n is the background noise contribution, which is defined as:

$$n = b(\frac{t}{10^{-3}})^{-\frac{1}{2}} \quad (16)$$

Where, b is the noise level at 1 ms. It is typically taken between 1 nV/m² and 5 nV/m² [42]. For some models, the forward data

and the data after noise addition are shown in Fig. 4.

C. Train

During training, the DR Block was set to 12, the batch size was set to 32, and AdamW was used as the optimizer with a learning rate of 0.0001. The training was conducted for 200 epochs on an Nvidia A6000 GPU.

We selected three methods for comparative analysis: TEMDnet [24], TEMSGnet [27], and TEM1Dformer [25]. TEMDnet represents convolutional and fully connected approaches, transforming one-dimensional signals into two-dimensional formats and applying image denoising techniques for noise reduction. The authors of TEMDnet have made their code publicly available on GitHub, which we used for training. TEMSGnet exemplifies generative methods, using noisy signals as conditional inputs to enable the diffusion model to generate clean signals conditionally. We trained

Fig. 8. The coordinates of the center point of the line source in the field exploration area are 95°90'30.55"N and 41°01'40.60"E.

TABLE I
COMPARISON OF FOUR DENOISING NETWORKS ON THE SIMULATION DATASET.

	MSE	SNR	SSIM
TEMDnet	3.9748e-4	36.0067	0.9499
TEMSGnet	9.6898e-5	43.7438	0.9810
TEM1Dformer	8.5346e-5	44.2069	0.9823
DREMnet	**1.8061e-5**	**47.4325**	**0.9959**

TEMSGnet using the code provided by its authors on GitHub. TEM1Dformer embodies transformer-based methods that utilize attention mechanisms, employing the vision transformer (ViT) encoder structure in its network architecture. Although the authors have not released their code, we replicated their approach based on ViT's code structure and use the settings outlined in their paper during training. Throughout the training process, we ensured that all methods utilized the same dataset and same training costs.

D. Test

1) Synthetic data: To verify that the encoder E correctly disentangles the data into content and context factors, we analyzed a set of clean and noisy signals and conducted a statistical analysis on the test set, as shown in Fig. 5. The clean signal s is disentangled into content factors Z_s^1 and context factors Z_n^1, while the noisy signal n is disentangled into content factors Z_s^2 and context factors Z_n^2. Decoding (Z_s^2, Z_n^1) with G_s, as shown in Fig. 5(a), accurately reconstructs the clean signal. Similarly, decoding (Z_s^1, Z_n^2) with G_n, as illustrated in Fig. 5(b), successfully reconstructs the noisy signal. These results demonstrate that the model can effectively disentangle the data. Additionally, we computed the MSE histogram between the decoded data from (Z_s^1, Z_n^2) and the noisy signal across the test set, as shown in Fig. 5(c). The results indicate that the network exhibits stable disentanglement performance, successfully separating data into content and context factors.

To evaluate the effectiveness of our method, we conducted tests on the test set, and the results are presented in Fig. 6. As shown, our method closely aligns with the theoretical clean data. In contrast, TEMDnet, based on convolution, and TEMSGnet, which uses a generative model, exhibit the largest deviation from the theoretical data due to their limited temporal awareness. Although TEM1Dformer, a transformer-based model, demonstrates improved temporal perception, its performance is slightly inferior to that of our proposed method.

To quantitatively evaluate the performance of the four methods, we calculated three evaluation metrics, as shown

in Table I. The results indicate that our method's denoising outcome is the closest to the theoretical signal, achieving the highest SNR. In contrast, the CNN-based method performed the worst, likely due to the inherent modeling limitations of convolutional networks.

To evaluate the stability of the proposed method, we conducted a statistical analysis on the entire test set, as shown in Fig. 7. Fig. 7 (a) presents the MSE histogram, where the results of DREMnet are concentrated around 1×10^{-5}, indicating smaller values compared to other methods. This suggests that DREMnet offers superior denoising performance with stable results. Fig. 7 (b) displays the SNR histogram, where DREMnet's results are concentrated around 45, achieving a higher SNR than the other methods.

2) Field data: To evaluate the model's denoising capability on field signals, we conducted a denoising experiment using field data collected from a survey area in Gansu, China, as shown in Fig. 8. The blue lines in the figure represent the survey lines, while the red line is the line source with a length of 2000 m. The transmitter model used is TXU30. The receiver operated at a flight altitude of 30 m, with a flight speed of 5 m/s and a sampling frequency of 192 kHz.

We directly applied the model trained on synthetic data to denoise the field data. Fig. 9 presents the denoising results for survey line 6. As shown, although TEMDnet and TEMSGnet successfully reduced cross-talk in some lower channels, they were unable to resolve it in the upper channels, and some noise remained in the lower channels. TEM1Dformer also showed room for improvement in denoising the lower channels. In contrast, DREMnet demonstrated the best performance, effectively eliminating cross-talk across all channels, providing clear signal contours, and significantly reducing noise in the lower channels, resulting in a smoother attenuation curve.

Fig. 10 presents the denoising results at the 20th, 40th, 60th, and 80th measurement points along survey line 6. As shown, the results processed by DREMnet exhibit a smoother attenuation curve, even in the later stages. In contrast, the denoising results from other neural networks still show some oscillations in the later stages of the curve. To further evaluate the denoising performance of the methods, we performed inversion [43] on the denoised results. The inversion results are shown in Fig. 11. As observed, the results processed by DREMnet more accurately reflect the geoelectric structure, while the inversion results of other methods display relatively blurred boundaries. In the high-resistivity region on the right side of the figure, DREMnet's results exhibit higher resolution, clearer boundary information, and a more continuous transverse direction, indicating a higher SNR in the data processed
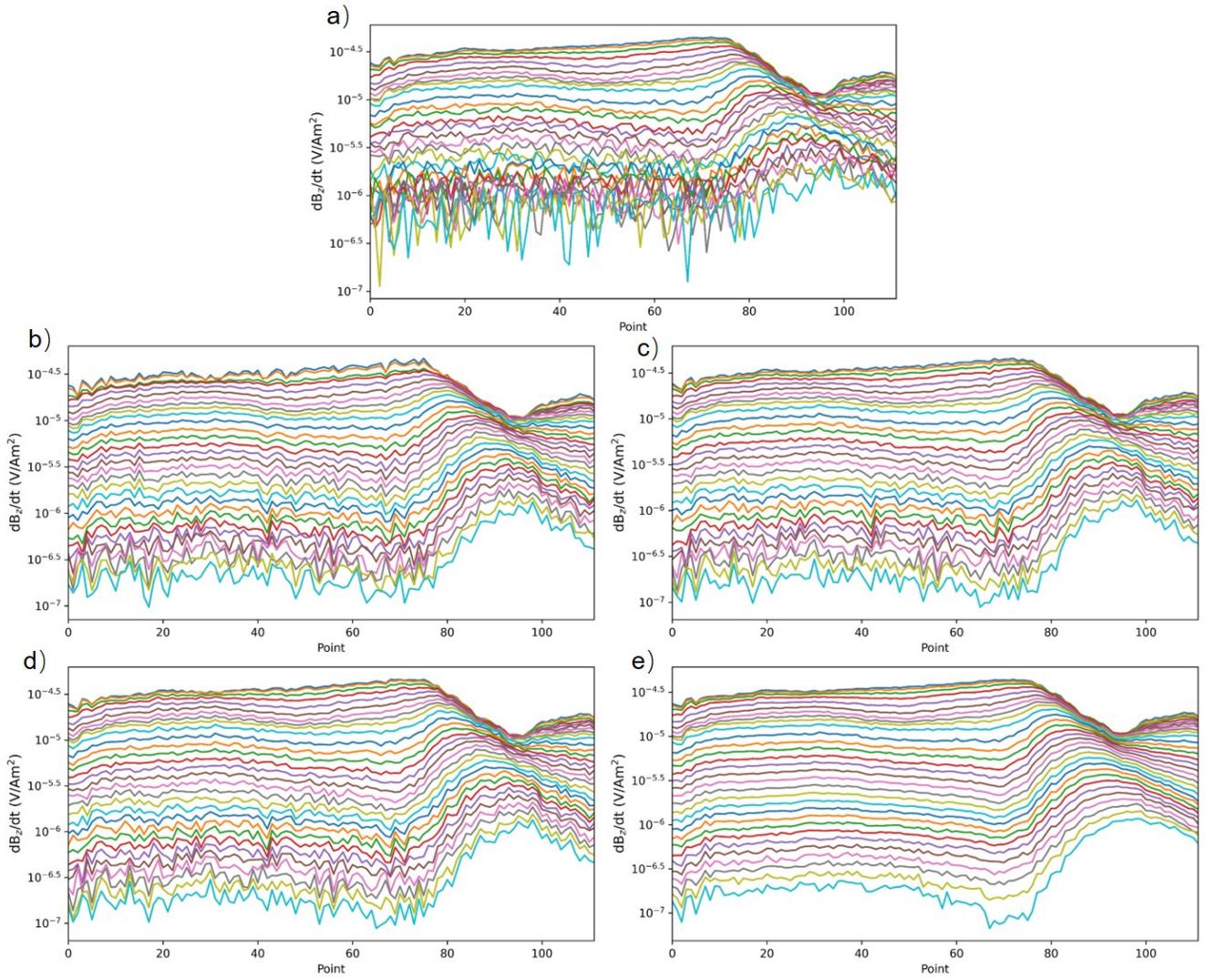
Fig. 9. The denoising results for survey line 6 are as follows: (a) represents the field data, (b) is the denoising result from TEMDnet, (c) is the denoising result from TEMSGnet, (d) is the denoising result from TEM1Dformer, and e is the denoising result from DREMnet.
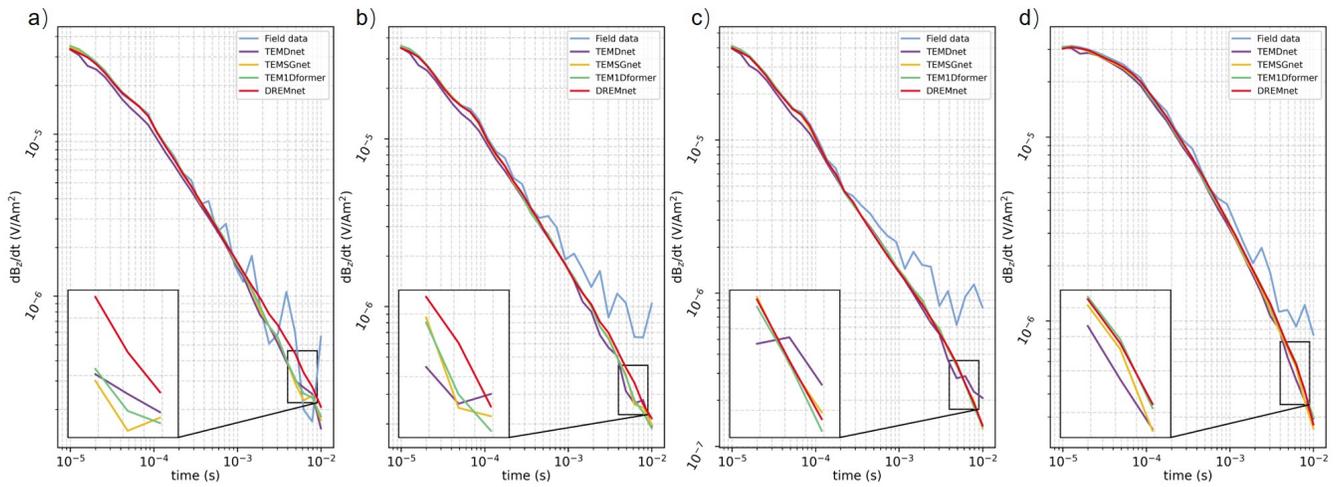

Fig. 10. (a) corresponds to measurement point 20, (b) corresponds to measurement point 40, (c) corresponds to measurement point 60, (d) corresponds to measurement point 80.
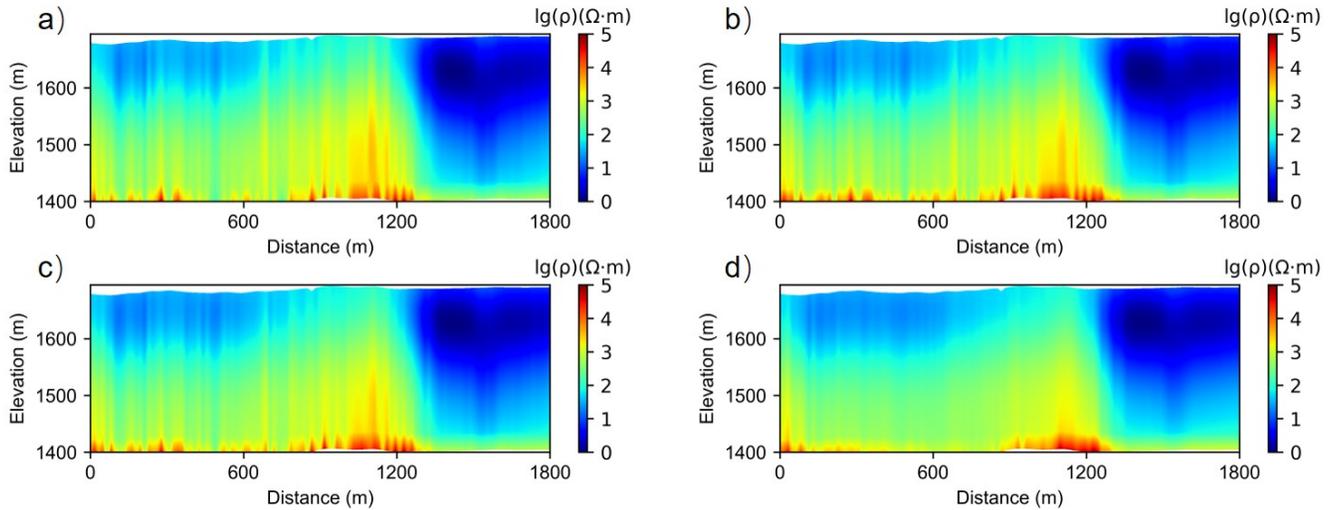
Fig. 11. The inversion results of survey line 6: (a) TEMDnet denoising result, (b) TEMSGnet denoising result, (c) TEM1Dformer denoising result, (d) DREMnet denoising result.

by DREMnet.

IV. CONCLUSIONS

This paper presents an interpretable framework for SATEM signal denoising based on disentangled representation learning. By leveraging this approach, the data is decomposed into content and context factors, facilitating robust and interpretable denoising of SATEM signals under complex conditions. The proposed method utilizes the RWKV architecture, overcoming the limitations of CNNs and transformers while retaining their advantages. Experiments on synthetic datasets demonstrate that the method outperforms others in denoising performance and effectively denoises field data using a model trained on synthetic data. The inversion results of the processed field data show that the proposed method yields results closer to the theoretical signal, offering a more accurate representation of subsurface features.

REFERENCES

[1] C. Chen and H. Sun, "Characteristic analysis and optimal survey area definition for semi-airborne transient electromagnetics," *Journal of Applied Geophysics*, vol. 180, p. 104134, 2020. I

[2] X. Wu, G. Xue, G. Fang, X. Li, and Y. Ji, "The development and applications of the semi-airborne electromagnetic system in china," *Ieee Access*, vol. 7, pp. 104 956–104 966, 2019. I

[3] P. Elliott, "New electromagnetic method provides fast deep-target data turnaround," *The leading edge*, vol. 15, no. 4, pp. 309–310, 1996. I

[4] T. Mogi, K. Kusunoki, H. Kaieda, H. Ito, A. Jomori, N. Jomori, and Y. Yuuki, "Grounded electrical-source airborne transient electromagnetic (greatem) survey of mount bandai, north-eastern japan," *Exploration Geophysics*, vol. 40, no. 1, pp. 1–7, 2009. I

[5] Y.-J. JI, Y. WANG, J. XU, F.-D. ZHOU, S.-Y. LI, Y.-P. ZHAO, and J. LIN, "Development and application of the grounded long wire source airborne electromagnetic exploration system based on an unmanned airship," *Chinese Journal of Geophysics*, vol. 56, no. 11, pp. 3640–3650, 2013. I

[6] H. Ito, T. Mogi, A. Jomori, Y. Yuuki, K. Kiho, H. Kaieda, K. Suzuki, K. Tsukuda, and S. A. Allah, "Further investigations of underground resistivity structures in coastal areas using grounded-source airborne electromagnetics," *Earth, Planets and space*, vol. 63, pp. e9–e12, 2011. I

[7] D. Li, Y. Wang, J. Lin, S. Yu, and Y. Ji, "Electromagnetic noise reduction in grounded electrical-source airborne transient electromagnetic signal using a stationarywavelet-based denoising algorithm," *Near Surface Geophysics*, vol. 15, no. 2, pp. 163–173, 2017. I

[8] Y. Ji, Q. Wu, Y. Wang, J. Lin, D. Li, S. Du, S. Yu, and S. Guan, "Noise reduction of grounded electrical source airborne transient electromagnetic data using an exponential fitting-adaptive kalman filter," *Exploration Geophysics*, vol. 49, no. 3, pp. 243–252, 2018. I

[9] F. Liu, J. Li, L. Liu, L. Huang, and G. Fang, "Application of the eemd method for distinction and suppression of motion-induced noise in grounded electrical source airborne tem system," *Journal of Applied Geophysics*, vol. 139, pp. 109–116, 2017. I

[10] Y. Ji, D. Li, M. Yu, Y. Wang, Q. Wu, and J. Lin, "A de-noising algorithm based on wavelet threshold-exponential adaptive window width-fitting for ground electrical source airborne transient electromagnetic signal," *Journal of Applied Geophysics*, vol. 128, pp. 1–7, 2016. I

[11] Q. Wu, Y. Ma, D. Li, Y. Wang, and Y. Ji, "Denoising algorithm of ground-airborne time-domain electromagnetic method based on variational bayesian-based adaptive kalman filter (vbakf)," *Journal of Applied Geophysics*, vol. 202, p. 104674, 2022. I

[12] J. Macnae and Y. Lamontagne, "Comparison of apparent resistivity functions for transient electromagnetic methods-discussion," *Geophysics*, vol. 49, no. 3, pp. 312–313, 1984. I

[13] J. C. Macnae, Y. Lamontagne, and G. West, "Noise processing techniques for time-domain em systems," *Geophysics*, vol. 49, no. 7, pp. 934–948, 1984. I

[14] K. McCracken, M. Oristaglio, and G. Hohmann, "Minimization of noise in electromagnetic exploration systems," *Geophysics*, vol. 51, no. 3, pp. 819–832, 1986. I

[15] P. Lv, X. Wu, Y. Zhao, and J. Chang, "Noise removal for semi-airborne data using wavelet threshold and singular value decomposition," *Journal of Applied Geophysics*, vol. 201, p. 104622, 2022. I

[16] H. Sun, C. Chen, Y. Yang, R. Lan, S. Deng, and D. Li, "Motion noise remove for secondary-field semi-airborne transient electromagnetic data," *Journal of Applied Geophysics*, vol. 202, p. 104676, 2022. I

[17] Y. Yang, H. ZHANG, C. ZHOU, C. CHEN, and H. SUN, "Motion noise removal method of semi-airborne transient electromagnetic pure secondary field data based on least square inversion," *Chinese Journal of Geophysics*, vol. 65, no. 6, pp. 2351–2364, 2022. I

[18] Z. Ma, Q. Di, Y. Jia, Y. Gao, and Y. Gou, "Receiver noise correction in semi-airborne transient electromagnetic method with an electric source," *Journal of Applied Geophysics*, vol. 211, p. 104955, 2023. I

[19] X. Wu, G. Xue, P. Xiao, J. Li, L. Liu, and G. Fang, "The removal of the high-frequency motion-induced noise in helicopter-borne transient electromagnetic data based on wavelet neural network," *Geophysics*, vol. 84, no. 1, pp. K1–K9, 2019. I

[20] K. Zhang, W. Zuo, S. Gu, and L. Zhang, "Learning deep cnn denoiser prior for image restoration," in *Proceedings of the IEEE conference on computer vision and pattern recognition*, 2017, pp. 3929–3938. I

[21] S. Potluri, A. Fasih, L. K. Vutukuru, F. Al Machot, and K. Kyamakya, "Cnn based high performance computing for real time image processing on gpu," in *Proceedings of the Joint INDS'11 & ISTET'11*. IEEE, 2011, pp. 1–7. I

[22] K. Zhang, W. Zuo, and L. Zhang, "Deep plug-and-play super-resolution for arbitrary blur kernels," in *Proceedings of the IEEE/CVF conference on computer vision and pattern recognition*, 2019, pp. 1671–1681. I

[23] J. Long, E. Shelhamer, and T. Darrell, "Fully convolutional networks for semantic segmentation," in *Proceedings of the IEEE conference on computer vision and pattern recognition*, 2015, pp. 3431–3440. I

[24] K. Chen, X. Pu, Y. Ren, H. Qiu, F. Lin, and S. Zhang, "Temdnet: A novel deep denoising network for transient electromagnetic signal with signal-to-image transformation," *IEEE Transactions on Geoscience and Remote Sensing*, vol. 60, pp. 1–18, 2020. I, III-B, III-C

[25] D. Pan, T. Qi, G. Feng, H. Wang, Z. Zhang, and X. Wei, "Tem1dformer: A novel one-dimensional time series deep denoising network for tem signals," *IEEE Sensors Journal*, 2023. I, III-C

[26] A. Dosovitskiy, "An image is worth 16x16 words: Transformers for image recognition at scale," *arXiv preprint arXiv:2010.11929*, 2020. I

[27] F. Deng, B. Wang, P. Jiang, X. Wang, and M. Guo, "Semi-airborne transient electromagnetic denoising through variation diffusion model," *IEEE Transactions on Geoscience and Remote Sensing*, 2024. I, III-C

[28] J. Ho, A. Jain, and P. Abbeel, "Denoising diffusion probabilistic models," *Advances in neural information processing systems*, vol. 33, pp. 6840–6851, 2020. I

[29] T. Lin, J. Yang, X. Lin, Y. Zhang, and T. Fan, "Semi-airborne electromagnetic line signal denoising based on recurrent self-coding neural network," *IEEE Transactions on Geoscience and Remote Sensing*, 2024. I

[30] Y. Liang, J. Fan, X. Zheng, Y. Wang, L. Huangfu, V. Ghavate, and Z. Yu, "An interpretable image denoising framework via dual disentangled representation learning," *IEEE Transactions on Intelligent Vehicles*, 2023. I

[31] S. Wang, F. Deng, P. Jiang, Z. Gong, X. Wei, and Y. Wang, "Seisfusion: Constrained diffusion model with input guidance for 3-d seismic data interpolation and reconstruction," *IEEE Transactions on Geoscience and Remote Sensing*, vol. 62, pp. 1–15, 2024. I

[32] H. Hou and F. R. Yu, "Rwkv-ts: Beyond traditional recurrent neural network for time series tasks," *arXiv preprint arXiv:2401.09093*, 2024. I

[33] B. Peng, D. Goldstein, Q. Anthony, A. Albalak, E. Alcaide, S. Biderman, E. Cheah, T. Ferdinan, H. Hou, P. Kazienko *et al.*, "Eagle and finch: Rwkv with matrix-valued states and dynamic recurrence," *arXiv preprint arXiv:2404.05892*, 2024. I

[34] B. Peng, E. Alcaide, Q. Anthony, A. Albalak, S. Arcadinho, S. Biderman, H. Cao, X. Cheng, M. Chung, M. Grella *et al.*, "Rwkv: Reinventing rnns for the transformer era," *arXiv preprint arXiv:2305.13048*, 2023. I

[35] K. Zhang, W. Zuo, Y. Chen, D. Meng, and L. Zhang, "Beyond a gaussian denoiser: Residual learning of deep cnn for image denoising," *IEEE transactions on image processing*, vol. 26, no. 7, pp. 3142–3155, 2017. II-A

[36] X. Wang, H. Chen, Z. Wu, W. Zhu *et al.*, "Disentangled representation learning," *IEEE Transactions on Pattern Analysis and Machine Intelligence*, 2024. II-A

[37] P. Cheng, W. Hao, S. Dai, J. Liu, Z. Gan, and L. Carin, "Club: A contrastive log-ratio upper bound of mutual information," in *International conference on machine learning*. PMLR, 2020, pp. 1779–1788. II-A

[38] Z. Yang, H. Zhang, D. Zhao, B. Wei, and Y. Xu, "Restore-rwkv: Efficient and effective medical image restoration with rwkv," *arXiv preprint arXiv:2407.11087*, 2024. II-B

[39] Y. Duan, W. Wang, Z. Chen, X. Zhu, L. Lu, T. Lu, Y. Qiao, H. Li, J. Dai, and W. Wang, "Vision-rwkv: Efficient and scalable visual perception with rwkv-like architectures," *arXiv preprint arXiv:2403.02308*, 2024. II-B

[40] M. R. Asif, N. Foged, T. Bording, J. J. Larsen, and A. V. Christiansen, "Dl-rmd: a geophysically constrained electromagnetic resistivity model database (rmd) for deep learning (dl) applications," *Earth System Science Data*, vol. 15, no. 3, pp. 1389–1401, 2023. III-B

[41] Y. Liu, Y. Zhang, C. Guo, S. Zhang, H. Kang, and Q. Zhao, "A multi-task learning network based on transformer network for airborne electromagnetic detection imaging and denoising," *Journal of Geophysics and Engineering*, p. gxae054, 2024. III-B

[42] E. Auken, A. V. Christiansen, L. H. Jacobsen, and K. I. Sørensen, "A resolution study of buried valleys using laterally constrained inversion of tem data," *Journal of Applied Geophysics*, vol. 65, no. 1, pp. 10–20, 2008. III-B, III-B

[43] J. Lu, X. Wang, Z. Xu, M. S. Zhdanov, M. Guo, M. Teng, and Z. Liu, "Quasi-2-d robust inversion of semi-airborne transient electromagnetic data with ip effects," *IEEE Transactions on Geoscience and Remote Sensing*, vol. 60, pp. 1–10, 2022. III-D2